Solar Energy Materials & Solar Cells 232 (2021) 111347

Contents lists available at ScienceDirect

Solar Energy Materials and Solar Cells

journal homepage: www.elsevier.com/locate/solmat

C_3N_4 interlayer formation while synthesizing black titania and their dye sensitized solar cell and conductivity performances

Nada A. Azab, Abdel-Azem M. El-Sharkawy, Z.A. Omran, W.A.A. Bayoumy, Mohamed Mokhtar *

Benha University, Faculty of Science, Chemistry Department, Benha, Egypt

ARTICLE INFO

Keywords:
Black titania
Evolution of C_3N_4
DSSC
Conductivity
Active sites

ABSTRACT

Black titania is an attractive applicant as a narrow bandgap absorber in photovoltaic cells. However, the non-equivalency between the amount of visible light absorbed and the photocatalytic activities limits its usage as photoanodes in the dye sensitized solar cells (DSSCs). Herein, the synthesized black titania (BT) via imidazole at 400°C; without washing steps, produces not only Ti_2O_3 and Ti_3O_5 nanoparticles but also allows the formation of the C_3N_4 nanosheets; which is emphasized via XRD, TEM-SAED-IFFT, FTIR, CV and XPS studies. The BT incorporated with hole transporting metals including Ag_2O, CuO and Ag_2S; at 3% loading, synthesized by deposition precipitation route are also fabricated to form p-n junction interfaces. The best conversion efficiency attained when using Ag_2O/BT was 6%; that presented the highest IPCE% in the visible light margin of 500–750 nm, followed by CuO (5.6%) and BT (4.9%). Although Ag_2O/BT did not absorb visible light as CuO, however, it offers minimum optical and electronic losses. Besides, it gives the highest dielectric constant (ε') value subsequent BT and exposes numerous active sites. Well correlations with vibrational, surface texturing, permittivity and electrical conductivity were achieved and discussed to have a view on the effect of the C_3N_4 interface as well as oxygen defect sites and the incorporation with metal oxide/sulfide groups. This work supplies a new aspect in the synthesis of g-C_3N_4 while synthesizing the oxygen deficient TiO_{2-x} in solar energy conversion reactions.

1. Introduction

The emergence of black TiO_2 (BT) nanomaterial has initiated wide-ranging study interest, as a result of its significantly enhanced solar absorption and the boosted photocatalytic activities. The development of the BT has been aroused to overcome the constriction of white TiO_2 such as wide band gap and fast charges recombination. Different synthetic approaches of BT are outlined on which some small variations are depicted [1–3]. These include structural, chemical characteristics, electrical conductivity and band structures. The BT nanomaterials have been applied in vast areas including visible-light photocatalysis, photovoltaics, photo-electrochemistry and chemical sensors [4]. The interest in BT is that it contains considerable defect numbers by which absorption of the visible light is initiated to facilitate many photo-assisted renewable energy applications [5–7]. It has been addressed before that the created Ti^{3+} in place of Ti^{4+}, produces a polaron (unpaired electron) [8]; as a result of the latter atoms reduction, capable of hoping from and to other Ti sites to intensify electricity. The accompanied simultaneous change in the electronic states produces color centres whom responsible for the light absorption property. On the other hand, oxygen vacant sites interact with each other, and with oxygen atoms on adjacent surface planes, to form unmanageable amorphous defect positions [9].

Although of the mentioned BT characteristics, the obtained results from whatsoever the applications (e.g., photovoltaics, and water splitting) are still beyond the expected ones. This is because the BT charges separation are not well managed beside the issue concerning that the amount of light absorbed is not well converted into the equivalent photocatalytic activity [10,11]. Accordingly, creating the right defects in the BT to manage both the chemistry motivated by light and electricity is critical query. Nevertheless, to solve such mismatching in the BT especially that demonstrated between the improved amounts of visible light absorption, band gap narrowing and the production of decreased equivalent photocatalytic activities is to dope it with p-type transition metals e.g., Ag_2O, Ag_2S and CuO. This design is expected to improve charge transport and recombination suppression when they used as photoanode materials in the dye sensitized solar cell (DSSC) application. Accordingly, we present a simple and competent route to

* Corresponding author.;
E-mail address: mohamed.mokhtar@fsc.bu.edu.eg (M. Mokhtar).

https://doi.org/10.1016/j.solmat.2021.111347
Received 11 June 2021; Received in revised form 6 August 2021; Accepted 19 August 2021
Available online 31 August 2021

fabricate BT containing Ti_2O_3, Ti_3O_5 and C_3N_4 structures for the first time as a consequence of the imidazole reduction at 400°C. Incorporation of Ag and Cu moieties may regulate the recombination process of the substantial defects localized on Ti surfaces together with C_3N_4 that may well shorten charge-to-surface migration distance in the perpendicular plane route.

2. Experimental

2.1. Chemicals and materials

Titanium dioxide (TiO_2, 99.00%) was purchased from Alpha Chemika, imidazole ($C_3H_4N_2$, 99.00%) was purchased from Qualikems, ($Cu(NO_3)_2.3H_2O$, 99.00%) was purchased from SD Fine-Chem Limited. Silver nitrate ($AgNO_3$, 99.00%) was purchased from BDH, sodium hydroxide (NaOH, 97.00%) was purchased from SDFCL, polyvinylidene difluoride PVDF (-($C_2H_2F_2$)n-, 99.50%) was purchased from Sigma-Aldrich, thiourea (CH_4N_2S, 98%), hydrochloric acid (HCl, 37.00% ± 1.00%), ethanol (C_2H_5OH, 99.90%), and acetic acid (CH_3COOH, 80.00%) were procured from Adwic pharmaceutical and chemicals company. Fluorine doped tin oxide conducting glass (F/SnO_2) (FTO) with surface resistivity of 7Ω/sq and transmittance equals 80–82% was purchased from Sigma-Aldrich. The chemicals were of analytical grade, market-ably accessible and used without additional purification. Distilled water is used throughout the whole experiments.

2.2. Synthesis methods

2.2.1. Synthesis of black TiO_2 (BT)

Briefly, 2.00 g of TiO_2 Degussa (S_{BET} = 54 m^2 g^{-1} with anatase/rutile ratio of 3) was thoroughly mixed with 4.00 g imidazole. The mixed powder was placed in a porcelain crucible and 3 ml HCl of 37% solution was added. This paste was then annealed in a muffle oven at 350 °C for 2 h and at 400 °C for 1h at a ramp rate of 5 °C min^{-1}.

2.2.2. Synthesis of CuO incorporated black TiO_2

First, the as-synthesized black titania (BT- 1.94 g) was immersed into the $Cu(NO_3)_2.3H_2O$ (0.182 g-70 mL H_2O) solution followed by stirring and sonication for 1 h, to activate both the adsorption and diffusion of Cu ions into the BT pores. This product was then heated into 90◦C followed by injecting 1 ml acetic acid under frequent stirring. NaOH solution (0.2 M) was added drop wisely to the above suspension till pH∼12 with continuous stirring for 0.5 h and sonication for 2 h. Centrifugation and washing with ethanol and distilled water till pH∼7 was acquired for the product that was finally dried overnight at 90 °C.

2.2.3. Synthesis of Ag_2O incorporated black TiO_2

Similarly, 1.94 g BT was dipped in $AgNO_3$ (0.088 g-70H_2O) solution so as to give 3% Ag_2O that stirred for 1.0 h. NaOH solution (0.2 M) was added drop-wisely to the above slurry till pH∼12 with continuous sonication for 2 h subsequent to stirring for 0.5 h. This mixture was separated via centrifugation and washed with distilled water for numerous times till pH = 7 and finally dried overnight at 80 °C.

2.2.4. Synthesis of Ag_2S incorporated black TiO_2

In typical, the BT (1.94 g) dissolved in $AgNO_3$ (0.082 g-70H_2O) and stirred for 1 h was dispersed in 20 ml of 0.0108 g thiourea solution that was drop wisely added while continuous stirring. This mixture was sonicated for 3 h and then passed into a Teflon-stainless-steel autoclave and heated at 180 °C for 24 h. The product was then centrifuged and the attained powder was washed with distilled water several times and finally dried overnight at 90 °C.

2.3. Characterization

XRD patterns were determined using a GNR APD 2000 PRO X-ray diffractometer at 45 kV with Cu Kα radiation (λ = 0.154 nm) with the ramping rate of 5°/min. The materials morphologies (size & shape) were determined using HRTEM (FEI-Tecni G20) attached with the SAED technique working at a speed voltage of 200 kV. The FTIR spectra were measured using a test scan Shimadzu FTIR spectrometer employing a KBr technique in the 4000-250 cm^{-1} range. UV–Vis spectra were carried out using a JASCO spectrophotometer in the margin 200–1000 nm whereas, the E_g values were calculated via detecting the straight-line intercept in the low-energy arise of the draw of $\alpha h\nu = A(h\nu - Eg)^n$. The electrical conductivity of the catalyst electrodes was examined with a computerized LCR bridge (ISTEK LCR-8110G).

The photovoltaic efficiency measurements of the electrodes were carried out first by molding the nano-materials mix with 1.0 mL of ethanol on FTO conducting glass and then dried at 90°C for 0.5 h forming the photoanode electrodes. The electrodes of 10 mm thickness were then immersed in a N3 solution dye of 1 × 10^{-4} mol/L concentration for 24 h at ambient temperature, and then washed with ethanol. The counter electrode comprised of the identical FTO painted with a thin graphite film, was set clearly on the top of the dye-covered nanomaterial films (arithmetical area 1.0 cm^2) to conserve constant pressure, where the electrical connection was constructed across the glass border. An electrolyte containing 0.3 M/0.03 M of KI/I_2 dissolved in acetonitrile was introduced by a capillary press into the interelectrode gap. The I–V cell property was inspected; by applying an external bias to the cell and measuring the generated photocurrent with a Keithley model 2400 digital source meter, using an AM 1.5-G lamp of power, 100 mW cm^2. The solar cell efficiency (ηy) was calculated using the equivalence: $\eta y = V_{oc}\ I_{sc}\ FF/P_{in}$, where P_{in} is the incident light power. Monochromatic IPCE spectra were calculated with a regulated Si/Ge photodiode as a reference detector via using halogen and Xenon lamps in the wavelength from 250 to 850 nm. The converted current density into incident IPCE was computed using the equation of IPCE = ((1240/λ) (I/P_{in})) x 100, where P_{in} = 30 W. X-ray photoelectron spectroscopy was conducted using Kratos-Axis DLD spectrometer device provided with monochromatic Al Kα irradiation at 1486.60 eV. The binding energies of different elements were normalized using C 1s binding energy (284.6 eV) of standard hydrocarbons. Nitrogen sorptiometry measurements were carried out using BET Nova Touch technique to determine S_{BET}, pore volume and pore radius values beside pore size distribution spectra. CV sketches were achieved in the range of -0.3–1.6 V at an examining rate of 50 mV s^{-1} from an electrochemical work space (CHI-760).

3. Results and discussion

3.1. Bulk and morphological characteristics

The XRD results of black titania (BT) with CuO, Ag_2O and Ag_2S modified BT are presented in Fig. 1 in comparison with the P-25 mother

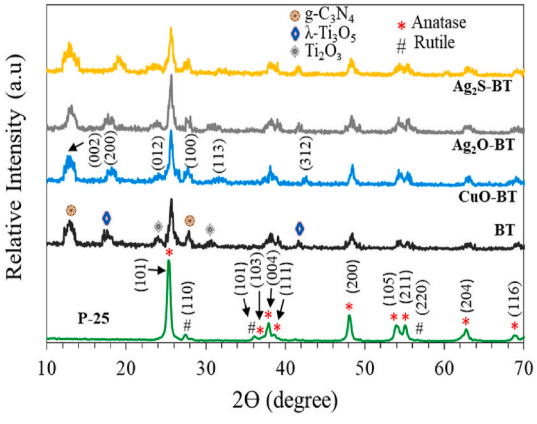

Fig. 1. XRD patterns of P-25, BT, CuO-BT, Ag_2O-BT and Ag_2S-BT samples.

sample to distinguish their bulk structures in the 2θ range extending from 10° to 70°. The BT pattern revealed the same peaks shown in the P-25; but at higher 2 theta angles, via exposing peaks (and crystal planes) at 2θ = 25.6° (101), 38.2 (004), 48.5 (200), 54.5 (105) and 55.7 (211), 63.3 (204) and 69.6° (116). A rutile peak at 27.6° (110) is depicted in the P-25 sample where a dissimilar feature peak at 27.8° is depicted in the BT probably of a different structure. An apparent decrease in anatase peaks intensities as well as shifts into higher 2 theta values was depicted besides an obvious widening of the (101) main anatase peak in the BT compared with the correspondent in the P-25 pattern. This indeed comprehends a decrease in the unit cell size implying deformation and decrease in the BT particles size with approved evolution of oxygen

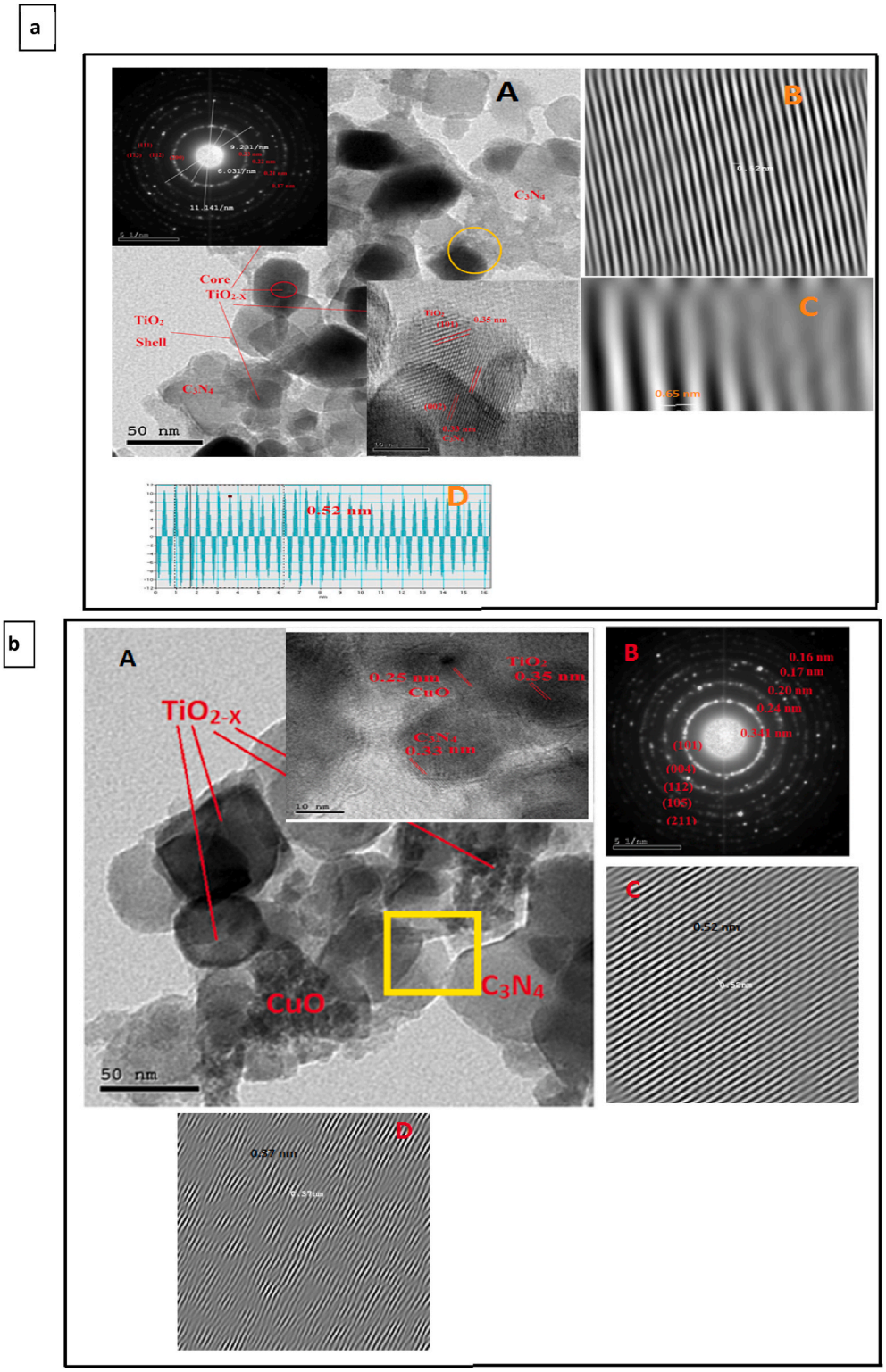

Fig. 2. The morphological and structural features of (a) the BT nanomaterials calcined at 400 °C with SAED ring and HRTEM image as inset (A) IFFT profiles of lattice spacing (B, C) and line profile fast Fourier transform and inverse fast Fourier transform (IFFT)) (D), (b) the TEM of CuO/BT beside the HRTEM as inset (A), SAED ring (B), and FFT lattice spacings (C, D).

vacancies pointing to disorder-produced lattice [12]. Another prominent peak at 2θ equal 17.65° assigned to the (200), facet is depicted characterizing the existence of the λ-Ti_3O_5 (PDF, No. 40–0806) component [13]. The distinct peaks seen in the BT at 2θ = 13° and 27.8° are probably correlated to the C_3N_4 structure [14]; as will be confirmed soon via TEM-SAED, FTIR and XPS analyses, describing the crystal planes (100) and (002), respectively. The latter peaks were not detected in neither titanate containing species nor other reduced titania entities. These peaks suffer shifting into higher 2θ following the metal incorporation, to indicate 13.2° and 27.85° values. This points to the involvement of the metals not only in the BT assembly but also in the carbon nitride structure. Other peaks at 2θ = 24.2° and 32.8° are also depicted characterizing the production of the more reduced form Ti_2O_3 (PDF, No. 43–1033) of (012) and (113) facets, respectively. This indicates the phase transformation of the TiO_2 anatase into Ti_2O_3/λ-Ti_3O_5 interfaces together with C_3N_4 those formed as a result of the imidazole interaction with the P-25 TiO_2 at a low temperature comprised of 400°C. The latter structure is probably formed as a result of creating both C and N atoms obtained a result of the imidazole disintegration; facilitated by conc. HCl addition. Rearrangement of the latter surface atoms so as to attain carbon nitride is expected putting into consideration that there is no washing step is provided. The anatase characteristic facet (101) beside the Ti_2O_3, λ-Ti_3O_5 and C_3N_4 phases presented shifts into higher 2θ values following incorporation of the metal oxides and sulfides within the BT compared with the metal free BT, characterizing a distortion (and rather oxygen vacancies in the BT lattice) based on increasing the atomic radii of the metal atoms (Ag and Cu) as well as increasing their electronegativity values compared to the Ti atom.

Indeed, synthesizing the polymorph anatase TiO_2 that includes Ti_2O_3 and λ-Ti_3O_5; of high-density oxygen vacancies, beside C_3N_4 might constitute all together a boost in the visible light absorptivity. Particularly, black λ-Ti_3O_5 and Ti_2O_3 those used to be synthesized using either carbothermal route or via hydrogen flow at high temperatures exceeding 1000°C [15]. For CuO, Ag_2O and Ag_2S modified BT samples; the XRD patterns show the presence of anatase peaks beside the binary Ti_2O_3/λ-Ti_3O_5 and C_3N_4 phases with the absence of any related peaks due to the corresponding oxides or sulfides emphasizing their dispersion. The crystallite diameter of the BT sample determined using the Scherer equation was 16 nm in comparison with 27.7 nm for the parent P-25. Whereas, the crystallite sizes of CuO, Ag_2S and Ag_2O modified BT indicate values composed of 18.6, 12.8 and 12.9 nm, respectively.

The TEM, HRTEM, SAED and IFFT images of the BT sample are illustrated in Fig. 2a. The TEM image shows shell spherical like shapes with black cores characterizing TiO_2 and TiO_{2-x} domains, respectively. They exhibit crystallite diameter of 28 nm and 15 nm, respectively. Apparently, dense layers of C_3N_4 are seen at the image corners. The HRTEM seen in Fig. 2A inset image depicted for the outlined yellow area is visualized and displayed the existence of lattice spacings, 0.35 nm and 0.33 nm validating the intimate interaction between the lattice spacing TiO_2 anatase (101) surface with the (002) surface of C_3N_4. The SAED analysis revealed the presence of several rings approving the polycrystalline nature of the BT sample. As can be seen in Fig. 2A inset, the obtained approximate interplanar spacings seen in the SAED matched up with XRD profile of the BT via exposing diffraction spots with plane lines (200) characteristic of C_3N_4 beside (112), (111) and (113) distinguishing TiO_2 and Ti_2O_3 oxides, respectively. The IFFT profile (Fig. 2B and C); performed to confirm spacing of the atomic planes, indicates d spacings at 0.52 nm and 0.65 nm denoting correspondingly the (200) plane of Ti_3O_5 and (100) plane of C_3N_4. The IFFT profile image seen in Fig. 2D also verifies the spacing 0.52 nm of the (200) surface affirming the presence of the Ti_3O_5 species, as previously described in the XRD profile. These complimentary results verify the BT heterogeneity and rather configure that it consists of suboxides comprised of Ti_2O_3 and Ti_3O_5 beside the C_3N_4 structural material.

The morphology of the CuO/BT sample studied by TEM, HRTEM, SAED and IFFT is illustrated in Fig. 2b. The TEM image exhibits multilayered sheets at the marginal part of the image characterizing the C_3N_4 structure where both CuO and TiO_{2-X} appeared as black spots in the TiO_2 matrix. Thus, to differentiate between them, the HRTEM is measured at some junction interfaces, as that yellow outlined square seen at the lower part of the image. It shows lattice fringe spacings at 0.33 nm due to the (002) crystal facet of C_3N_4, 0.35 nm caused by the crystal facet (101) of TiO_2 beside the spacing of 0.25 nm characterizing the (111) plane of the CuO structure. The SAED (2b-B) shows a series of spots with diffraction d spacing equal 0.341, 0.243, 0.20, 0.17 and 0.164 nm characterizing the planes (101), (004), (112), (105) and (211) of TiO_2. The IFFT images viewed in Fig. 2b (C&D) confirm the 0.52 nm spacing of the (200) facet of Ti_3O_5 as well as the spacing 0.37 nm corresponding to the (012) plane of Ti_2O_3 species.

3.2. Surface texturing

To comprehend to what extent, the surface properties of the synthesized catalysts affected the photovoltaic characteristics, N_2 adsorption isotherms and pore size distribution curves were measured for some representative samples (Fig. 3). The BT isotherm shows type II without any plateau characterizing the accessibility of various pore sizes. However, the absence of any hysteresis loop attained through the isotherm desorption branch realizes the predominance of micropore sizes. Similarly, CuO/BT indicates type II isotherm with a hardly depicted hysteresis in the p/p^o margin 0.4–0.8, illustrating the growth of mesopores as a result of the CuO incorporation. Concurrently, the CuO/BT sample indicates lower pore volume comprised of 0.038 ml/g in front of 0.041 ml/g for the BT sample. This indeed leads to a small decrease in the S_{BET} (21 m^2/g) of CuO/BT compared to that of the BT (25 m^2/g) with invariable pore radius values (~1.8 nm). The inset pore size distribution curves show a little widening toward the mesopores (1.8–7.4 nm) in the BT compared to CuO/BT that clarifies pore size limitation (1.8–4.8 nm). This clarifies that the dispersion of CuO nanoparticles inside the BT pores creates accessible nanopores for the I^-/I_3^- fast diffusion. The Ag_2S and Ag_2O samples incorporated BT show typical isotherm of CuO/BT except that Ag_2O/BT gives a little increase in the S_{BET} into 23 m^2/g and comparable pore volume as BT equal 0.041 ml/g.

3.3. Optical properties

The optical characteristics of the as-synthesized samples comprised of BT, CuO/BT, Ag_2O/BT, Ag_2S/BT in comparison with the P-25 mother sample are depicted in Fig. 4 with their energy band gaps calculation as inset. The BT sample shows an increased light absorption via exposing a peak maximized at 450 nm; which tailed till 800 nm, in comparison with an edge band at 390 nm for the P-25 sample. This presumes lattice disorder due to the increase in the Ti^{3+} concentration and O_2 vacancies and thus reduces its E_g value [16]. The band gaps analyzed via tauc plots for P-25, BT, CuO/BT, Ag_2S/BT and Ag_2O/BT were 3.15, 1.86, 1.68, 1.64 and 1.74 eV, respectively. The band gap narrowing is developed based on the evolution of sub-band locations of Ag^+ and Cu^{++} beside the oxygen defects. Decreasing the band gap of the Ag^+ moieties is correlated to increasing its ionic radius compared to Ti^{4+} or Ti^{3+} species and its possible migration into the latter surfaces producing Ag nanoparticles. The absorption spectrum of CuO/BT results in a broad peak at 480 nm that was comparable to that of Ag_2S/BT (480 nm) and rather they superimposed each other except that the former exceeded the later in the UV region. This explains that metal oxides/sulfides doped samples create electronic energy levels within the energy band gap [17]. Although the Ag_2O/BT spectrum exhibits a peak at 480 nm however, it shows a decrease in the visible light absorption compared to both CuO and Ag_2S doped BT samples. The peaks at 480 nm configured in all samples are mostly correlated to the metal oxide/sulfides coordinated BT (e.g., CuO–Ti) and not to the individual oxides (used to appear at 220–250 nm for CuO, 300 nm for Ag_2S) [18,19]. However, due to the peak broadness, plasmonic metal absorptions (used to occur at 568 nm

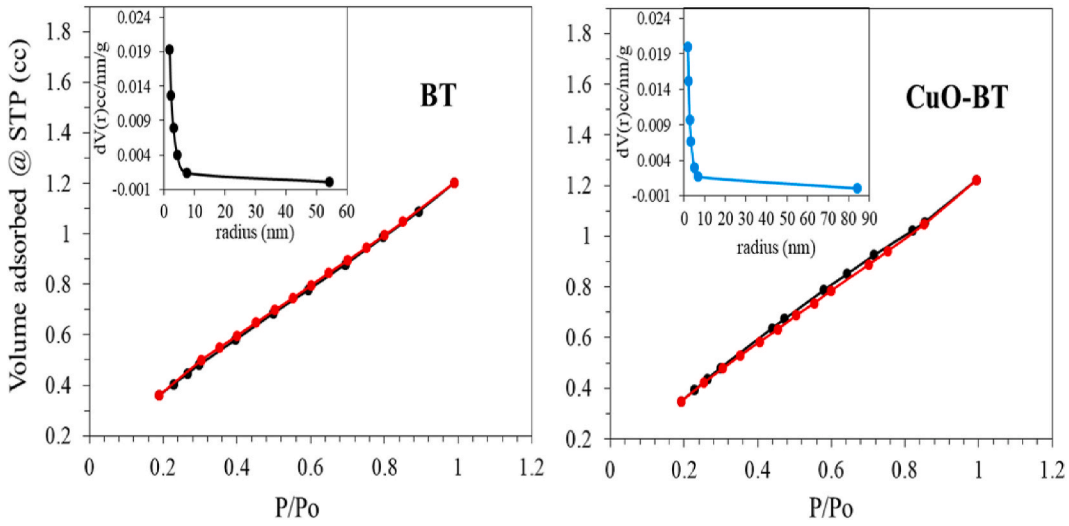

Fig. 3. Adsorption-desorption isotherms and pore size distribution curves (in-set) of BT, CuO-BT catalysts.

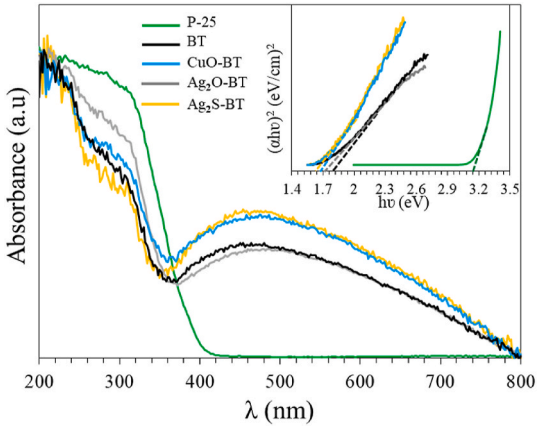

Fig. 4. Optical absorption spectra of P-25, BT, CuO-BT, Ag_2O-BT and Ag_2S-BT catalysts and in-set are their tauc plots.

for Cu and 425 nm for Ag) could be included beside the combined charge transfer processes of $O^{2-} \rightarrow Ti^{4+}$ and $O^{2-} \rightarrow Cu^{2+}$. Also, the peak broadness could also be an indicative of the suboxide attendance and the aforementioned exhibited decrease in particle sizes. The sample spectrum of Ag_2O/BT was also superimposed that of the BT in the visible margin however it exceeds that of the BT in the UV limits. Other peaks are significantly discerned in the spectra of the 260–300 nm margin and maximized at ~270 nm. Mostly, the latter peak is ascribed to the involvement of a more reduced TiO_{2-x} form.

3.4. Vibrational spectroscopy

The FTIR spectra of the BT and those of metal modified BT presented in Fig. 5 are displayed in the frequency range of 3900-400 cm^{-1}. The BT spectrum indicates new vibrational bands than those seen in the P-25 mother sample specifically in the margins 1200-1700 cm^{-1}, 400-700 cm^{-1}, and 3000-3900 cm^{-1}. The former margin indicates identifiable carbon nitride vibrational peaks at 1273, 1396, 1411, 1519, and 1620 cm^{-1} resemble to those of the C–N stretching vibrations. A small absorption peak at 864 cm^{-1} is also recognized and ascribed to the typical deformation mode of the N–H bonds [20]. Widening the absorption bands in the 3000-3900 cm^{-1} margin in the BT sample compared to the P25 sample via exposing peaks at 3749 cm^{-1} and 3402 cm^{-1}; in front of 3420 cm^{-1} for the latter, beside a shoulder at 3200 cm^{-1} are depicted. These ascribed in sequence to the terminal OH groups (3749 cm^{-1}), O–H stretching vibration (3420-3400 cm^{-1}) and N–H symmetric stretching vibration (3200 cm^{-1}). The band at 3749 cm^{-1} that never seen in P-25 is probably due to oxygen vacancies of the Ti^{3+} moieties. The BT spectrum shows shifts of the low frequency bands seen in the P-25 (490 and 665 cm^{-1}) spectrum; those ascribed respectively to Ti–O–Ti and Ti–O bonds, into 524 and 671 cm^{-1}, emphasizing their engagement to the Ti^{3+} moieties. In the CuO-BT spectrum new bands at 570 cm^{-1} and 502 cm^{-1} assigned to Cu–O–Ti and monoclinic CuO species [21] are depicted. Similarly, the Ag_2O-BT spectrum shows a band at 462 cm^{-1} due to Ag–O bonds beside a one at 918 cm^{-1} due to the Ti–O–Ag linkages [22]. Additionally, the BT band seen at 3749 cm^{-1} is shifted into 3765 cm^{-1} in Ag_2O-BT comprehending the involvement of the Ag^{+} species within the Ti^{3+} moieties. For the Ag_2S-BT spectrum, very small bands correlated to the symmetric S–O vibrations are appeared in the range 1041–1101 cm^{-1} [23] for Ag_2S, and rather established the Ti–O–Ag bond formation at 656 cm^{-1}. The broadness of the peak at 656 cm^{-1} overwhelmed the Ag–S band used to be seen in the 500-600 cm^{-1} margin. The bands in the margin from 1700 to 1200 cm^{-1} are significantly reduced in intensities as depicted in the Ag_2O-BT spectrum proposing a strong interaction of Ag^{+} with OH bending, C–N, C–OH and N–H vibrations. Additionally, shifting the band at 3749 cm^{-1} into 3765 cm^{-1} in both Ag_2O and Ag_2S confirms their strong interactions with the Ti^{3+} species that might stimulate the charge transfer process.

3.5. X-ray photoelectron spectroscopy

The survey spectrum of the BT sample consisting of Ti, O, N and C elements is presented in Fig. S1. The XPS spectrum of the Ti 2p element (Fig. 6) shows the existence of Ti^{4+} at binding energies of 458.8 eV and 464.6 eV correlated correspondingly to Ti 2p 3/2 and Ti 2p 1/2 beside two small peaks at 457.9 eV and 461.0 eV due to Ti^{3+} matching respectively to the same mentioned components [24]. Apparently, the Ti^{3+} represents 13.9% of the Ti^{4+} atomic percent ratio. The O1s spectrum of the BT is fitted into two peaks with binding energies at 530.2 eV and 532.3 eV correlated to Ti^{4+}-O (lattice oxygen) and Ti^{3+}-O, respectively [25]. The N1s doublet peak positioned at 398.5 and 399.8 eV is deconvoluted into three peaks at 400.8 eV, 399.8 eV and 398.3 eV due to N atoms attached to three carbon atoms –N<, sp^2 C= N- bond in the s-triazine ring and –NH- species of the C_3N_4 structure [26]. The XPS C1s spectrum that shows a peak at 284.8 eV is deconvoluted into three sub-peaks configuring carbon contamination at 284.7, 286.0, and 288.1 eV with atomic ratios equal 64, 24 and 12% respectively. These peaks are attributed respectively to C–C coordination, sp^2 bonded C in C=N

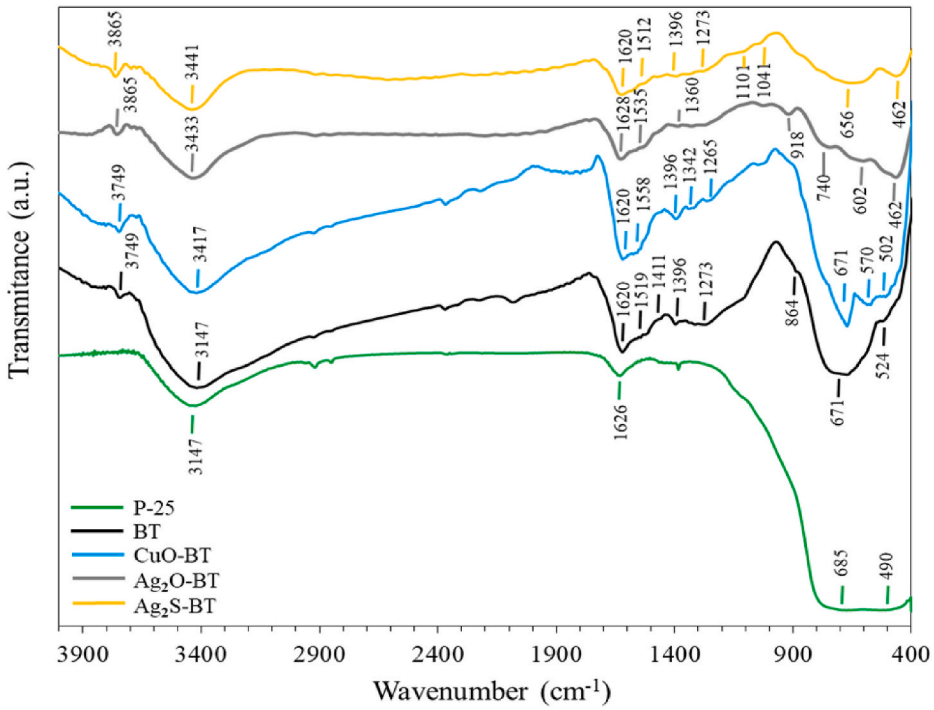

Fig. 5. FTIR spectra of P-25, BT, CuO-BT, Ag_2O-BT and Ag_2S-BT samples in the 400-4000 cm^{-1} range.

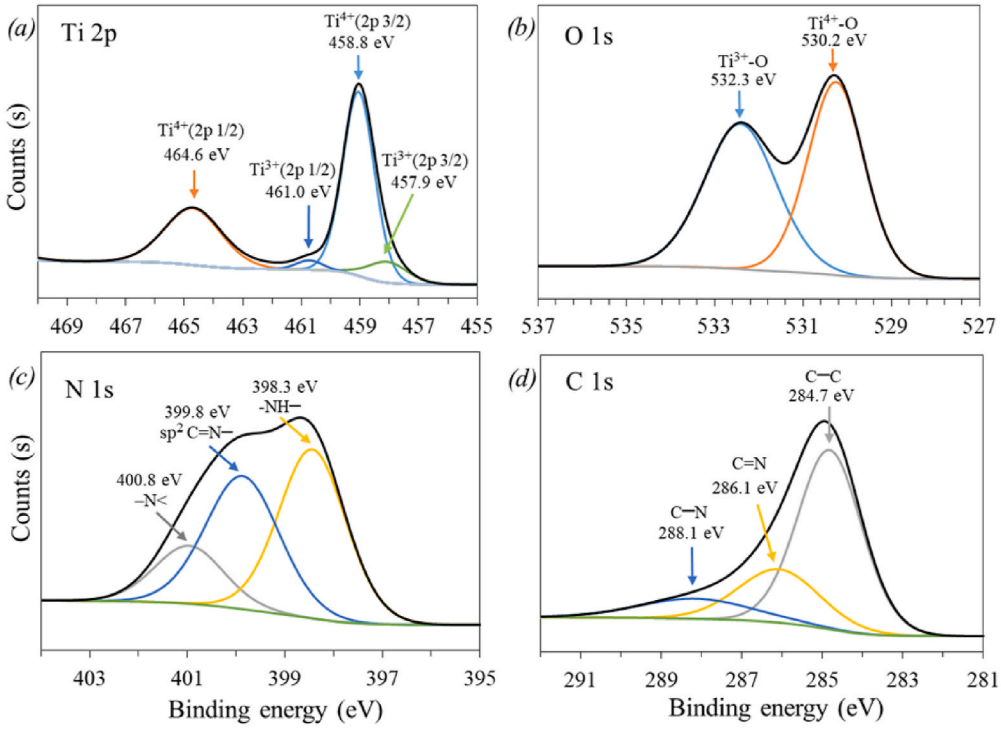

Fig. 6. High resolution XPS spectra of *(a)* Ti 2p, *(b)* O 1s, *(c)* N 1s, *(d)* C 1s in the BT catalyst.

and sp^3 bonded C in C–N of C_3N_4 [27]. The presence of peaks at 288.1 eV substantiates the formation of the carbon nitride. This verifies that the reduction of TiO_2 using imidazole at the specified conditions produces not only oxygen deficient TiO_{2-x} sites but also appreciable percentages of both carbon (44%) and nitrogen (13%) elements to specify the formation of C_3N_4.

On the other hand, the XPS survey spectrum of CuO incorporated BT depicted in Fig. S2 indicates the same elements as BT in addition to the Cu component. The Ti 2p spectrum indicates two main peaks at 458.3 and 464.3 eV; characterizing the Ti^{4+} species, those deconvoluted into 3 sub-peaks at 457.3, 460.4 and 462.5 eV to describe the existence of the Ti^{3+} moieties (Fig. 7). The percent ratio of the latter species was inferior (10%) than that depicted in the Cu free BT sample. A little shift into low binding energy values is depicted in the CuO/BT sample confirming the

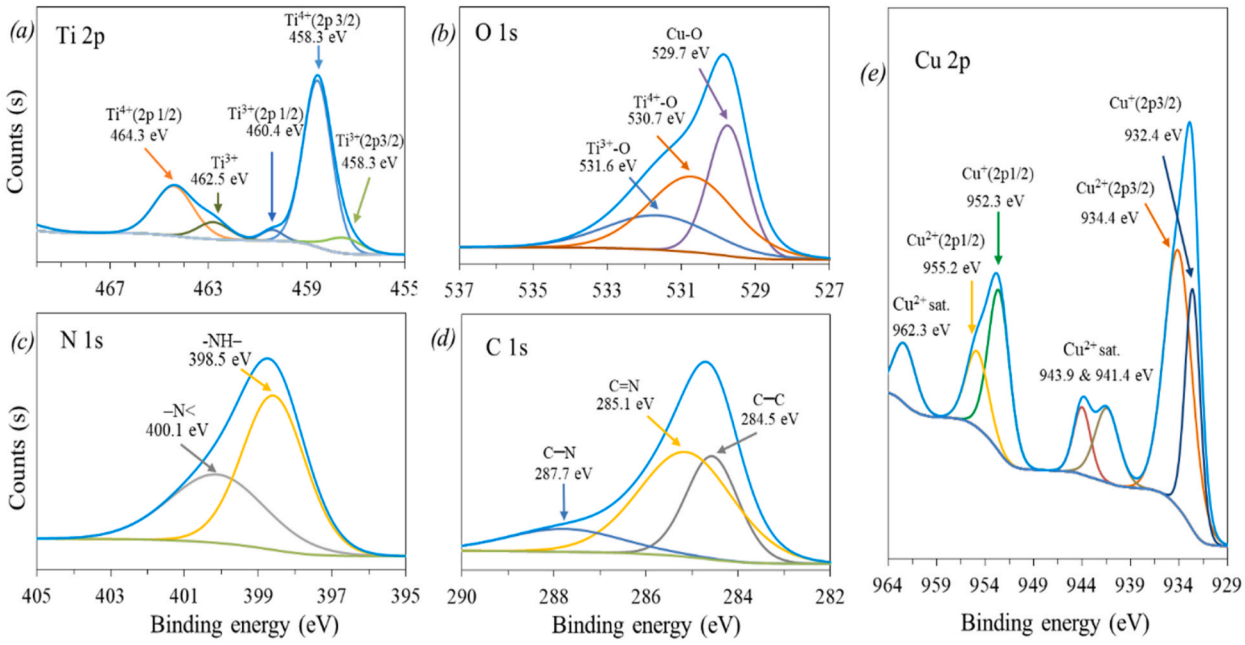

Fig. 7. High resolution XPS spectra of *(a)* Ti 2p, *(b)* O 1s, *(c)* N 1s, *(d)* C 1s, *(e)* Cu 2p in CuO-BT catalyst.

well incorporation of Cu ions in the TiO_{2-x} lattice structure and most probably replaces some of Ti^{4+} atoms. The O1s spectrum shows one broad peak; unlike the correspondent in the BT, at 529.8 eV that is analyzed into three peaks at binding energies 529.7, 530.7 and 531.6 eV. The latter peaks are assigned correspondingly to the oxygen in CuO [28], oxygen deficient Ti_2O_3 and the non-lattice oxygen [24]. The existence of the latter species confirms the increase of oxygen vacancies in the lattice when compared with the BT that it never existed. The N1s single peak positioned at 398.6 eV is deconvoluted into two sub-peaks at 398.5 and 400.1 eV illustrating the presence of –NH- and –N< bonds, respectively. The absence of the = N- bonds in this CuO/BT sample compared to the BT sample estimates the preferable interaction of Cu atoms via this type of linkage. The C1s spectrum exhibited as a major peak at 284.6 eV and deconvoluted to three sub-peaks at 284.5, 285.1 and 287.7 eV are depicted in Fig. 7. The later peaks are assigned typical to those seen in the C1s spectrum of the BT sample. The minor shift into lower binding energies of latter peaks is indicative to the Cu dispersion in TiO_2 substitutional positions. The Cu 2p spectrum shown in Fig. 7 indicates the binding energy of Cu 2p3/2 at 932.6 eV that fitted into two sub-peaks at 932.4 (17%) and 934.4 (35%) eV and ascribed to the

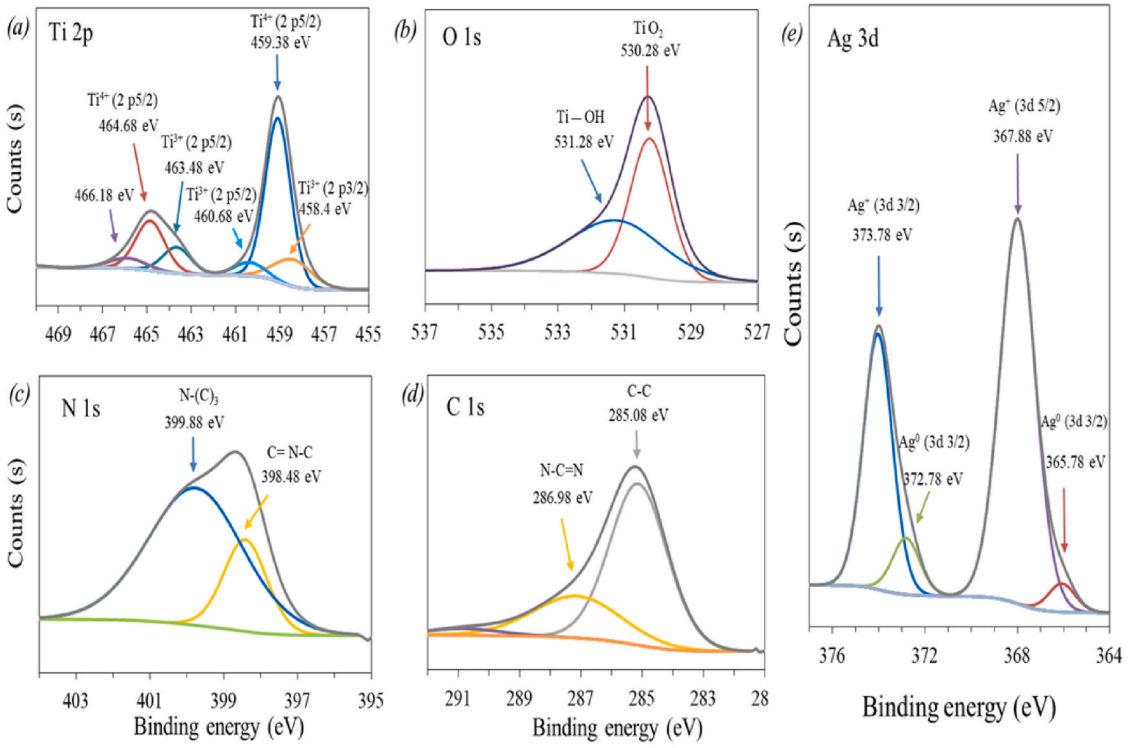

Fig. 8. High resolution XPS spectra of *(a)* Ti 2p, *(b)* O 1s, *(c)* N 1s, *(d)* C 1s, *(e)* Ag 3d in Ag_2O-BT catalyst.

attendance of Cu^{+} and Cu^{2+} states, respectively [29]. The latter peak is accompanied with two satellite peaks at 941.4 and 943.9 eV proposing the existence of the CuO moieties. Similarly, the Cu 2p1/2 peak positioned at 952.6 eV that deconvoluted into two peaks at 952.3 (17%) and 955.2 (8.6%) eV is validated to recognize the presence of Cu^{+} and Cu^{++}, respectively. At higher binding energy a satellite peak 962.3 eV to confirm the CuO formation is also seen. This XPS exploration reveals that N and C atoms are effectively integrated in the TiO_2 lattice structure and expected to provide additional active sites for the photovoltaic reaction. The dopants C (46%) and N (12%) are willing to from 2p electronic positions over the VB producing charge transfer transition to either V_Os Ti^{3+} or to copper (below the CB) incorporated TiO_{2-x} present close to the CB.

The surface states and atomic% concentration of the Ag_2O/BT composite measured using the XPS investigation are illustrated in Fig. 8 for the elements Ti 2p, Ag 3d, C1s, N1s and O1s. The Ti 2p spectrum indicates two main peaks at 459.38 eV; of Ti $2P_{2/3}$, and 464.68 eV; of Ti $2p_{1/2}$, for Ti^{4+} where they deconvoluted into additional two peaks at 458.4 eV and 460.68 eV for the former and 463.48 and 466.18 eV for the latter. This reflects the presence of Ti^{3+} species via evolution of the peaks at 463.48 eV (Ti^{3+} $2p_{1/2}$) and 458.4 eV (Ti^{3+} $2p_{3/2}$) constituting 15% of the total Ti^{4+} species. The evolution of the peak at 466.48 eV is probably attributed to the complex formation of Ti with Ag; that never existed in the BT Ti_{2p} XPS spectrum, whereas that at 460.68 eV is attributed to the core level Ti $2p_{3/2}$ of Ti^{4+} state. An increase in the binding energy is acquired for the Ti 2p main peaks following Ag_2O incorporation within BT when compared with the mother BT Ti 2p spectrum. The O1s spectrum gives peaks at 530.28 eV and 531.28 eV fitted to lattice oxygen of TiO_2 and Ti–OH moieties, respectively [30,31]. The XPS spectrum of N 1s shows typical two peaks as those resolved in the BT but at slightly higher binding energies at 398.48 eV and 399.88 eV; verifying the environment change and rather proposes the intense interaction between Ag_2O and BT, assigned respectively to the sp^2-hybridized aromatic (C= N–C), and tertiary nitrogen N-$(C)_3$ [32]. The absence of the peak at 400.8 eV seen in the BT advocates the probability of the Ag_2O interaction with the C–N–H groups. Compatibly, the C 1s spectrum indicates a peak at 385.08 eV due to the C–C linkages exceeding that of the BT (284.7 eV), and deconvoluted into another peak at 386.98 eV of N–C=N [33] shifted 0.88 eV following the Ag_2O involvement. This affirms the strong contact at the interface between BT (C_3N_4) and Ag_2O/Ag moieties. The spectrum of the Ag 3d exposes 2 main peaks at 367.88 and 373.78 eV correlated to Ag $3d_{5/2}$ and Ag $3d_{3/2}$ of Ag^{+} species and indicative of the Ag_2O existence [34]. They are further split up into two small peaks at 365.78 and 372.78 eV due to Ag nanoparticles [35,36] that constitutes 15% of the Ag_2O moieties. The existence of Ti^{4+}/Ti^{3+} and Ag^{+}/Ag ($Ag^{+} + Ti^{3+} \rightarrow Ag^{0} + Ti^{4+}$) in Ag_2O/BT could bring great advantages via facilitating the photogeneration of electron/hole carriers besides enhancing their transfer rate and recombination control. In addition, C_3N_4 can excite electrons upon illumination and considerably increases the conductivity of the material beside oxygen vacancies and Ag metal; which not only works as electron reservoir but easily can be oxidized to Ag^{1+}, that played a marked role in enhancing both the electron transfer and weakening their association again.

Based on the obtained results from XRD, TEM-SAED-IFFT, XPS and FTIR, the expected mechanism of the C_3N_4 evolution during the BT fabrication can be deduced as follows (Scheme 1).

3.6. Photovoltaic characteristics

The measured solar cell performances of CuO/BT, Ag_2O/BT and Ag_2S/BT photoelectrodes in comparison with the BT are depicted in Fig. 9. (a). Apparently, the Ag_2O/BT cell efficiency was the highest (6%) exceeding in sequence CuO/BT (5.6%), BT (4.9%) and Ag_2S/BT (no result). From the data seen in Table 1, it is clear that Ag_2O/BT gives the maximum value of I_{SC} (3.5 mA cm^{-2}) than rest of the electrodes as well as the highest I_{max} (2.7 mA cm^{-2}), whereas that of CuO/BT indicates the highest open-circuit voltage, (V_{OC}; 1.76 V), and similar fill factor (0.44) as the former but lower light generated current (I_{SC}; 3.2). These results indicate that Ag_2O/BT increases the electron transfer in the short circuit current density [36]. This explains that the heterostructure of P-type Ag_2O and CuO with n-type of BT facilities the electron donor density from the BT into the acceptor CuO and Ag_2O moieties. This indeed is emphasized by decreasing the work-function of titania especially after oxygen vacancy creation [37] (<4.2 eV) compared to both oxides (4·61 ± 0·04 for CuO and 4·35 ± 0·05 for Ag_2O). Optimizing the efficiency is much dependent on FF, I_{SC} and V_{OC} values those are correlated to the E_g values, carrier densities as well as their facile transfer rate. The analyzed E_g of CuO/BT and Ag_2O/BT were lower (1.68–1.74 eV) than that of the BT (1.86 eV), and thus imposes lower impedance characteristics for both solution and charge transfer resistances. The little increase in the V_{OC} of CuO/BT is indeed associated with increasing its E_g value; compared to Ag_2O/BT, and assumes the decrease in the recombination rate of charge carriers. Decreasing the efficiency alongside the latter parameters (FF, I_{SC} and V_{OC}) for the BT photoelectrode is mainly due to increasing the interface defects on which charges recombination are exhibited and thus affects electronic and optical characteristics. Despite that, our BT sample exhibited higher conversion efficiency (4.6%) than beta-voltaic black

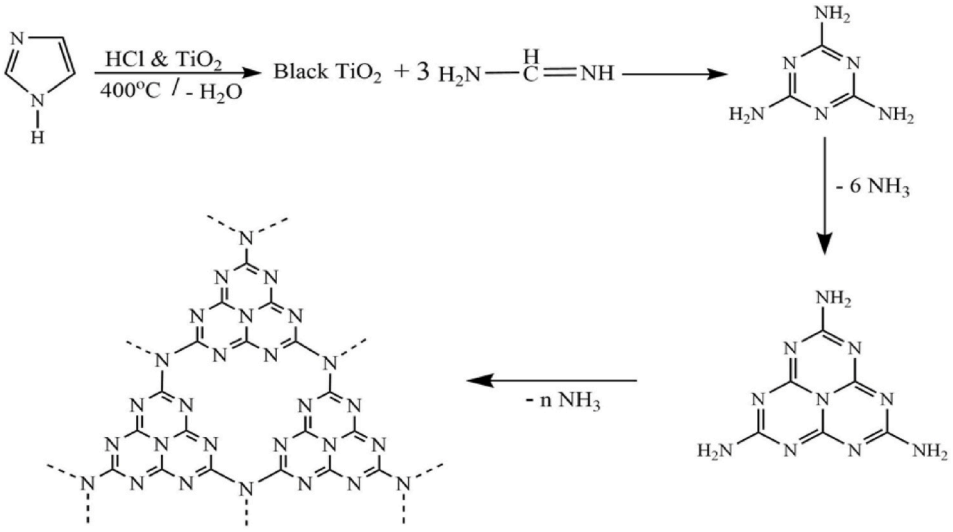

Scheme 1. Schematic illustration of the formation of C_3N_4 during synthesis of black titania.

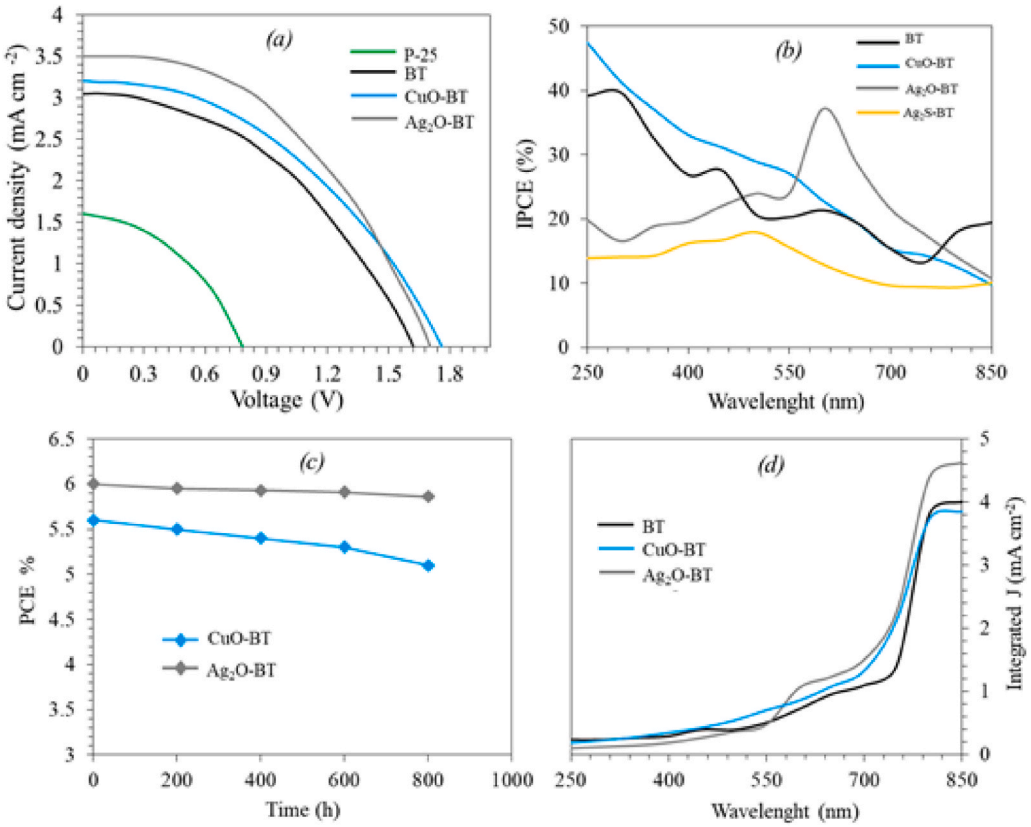

Fig. 9. *(a)* J-V curves of typical P-25, BT, CuO-BT and Ag_2O-BT DSSCs, *(b)* Incident-photon-conversion efficiencies, *(c)* Long-term stability of DSSC based on Ag_2O/BT and CuO/BT under visible-light irradiation, and *(d)* Integrated short circuit current of BT, CuO-BT and Ag_2O-BT solar cells based on N3 dye.

Table 1
Solar performance parameters of P-25, BT, CuO-BT, and Ag_2O-BT DSSCs.

Sample	V_{max}(V)	I_{max}(mA)	V_{oc}(V)	I_{sc}(mA)	FF	PCE (%)
P-25	0.462	1.12	0.78	1.6	0.414	1.2
BT	0.97	2.2	1.62	3.05	0.432	4.9
CuO-BT	1.08	2.3	1.76	3.2	0.441	5.6
Ag_2O-BT	0.97	2.7	1.7	3.5	0.44	6

nanotube titania (3.65%) [37]. This indeed is correlated to involvement of the C_3N_4 structure beside Ti^{3+} and oxygen vacancies, those capable of improving the charges separation. Increasing the PCE for the BT when compared with other black titanias [37,38] is attributed to the formed interface engineered with C_3N_4. Therefore, on the basis of excellent structure, electronic and optical properties of C_3N_4, its utilization in the photoelectric conversion field is highly appreciated. Because, it efficiently increases charges mobilities, decline energy barrier, boost charge transport, and retard charge recombination [14,32]. Moreover, the nitrogen sites of C_3N_4 make it nucleophilic, Lewis basic and easy to develop hydrogen bond.

The IPCE spectra to notify how considerably the absorbed light by the electrode is transformed into current are depicted in Fig. 9b in the wavelength range of 250–850 nm. Apparently, CuO/BT shows a monotonous decrease in the IPCE reaching 12% at 850 nm. The BT photoelectrode shows the same behavior as the CuO/BT one but at lower IPCE values till 625 nm, after which an overlaying on the former till 700 nm is approached followed by an increase beyond 740 nm till 850 nm. It's noteworthy mentioning that the CuO/BT photoelectrode gives the highest IPCE values throughout all the range from 250 to 550 nm proposing the role CuO and Cu_2O layers; emphasized from XPS results, those absorb more photons, to bring about increased photo-generated current. The Ag_2S/BT electrode shows the lowest IPCE values throughout all the wavelength range giving a maximum of 17% at 500 nm. The IPCE of Ag_2O/BT is greatly increased especially in the wavelength margin of 560–780 nm with a maximum at 625 nm to give an IPCE value of 40%. This evidences that increasing the PCE value of Ag_2O/BT together with the IPCE establishes that this specific photoelectrode absorbs the majority of light impinged into it followed in sequence by CuO/BT and BT. Conversely, although Ag_2S/BT presents appreciable absorption in the visible region exactly as CuO/BT however, it indicates no activity probably because of fast charges recombination by which it delivers the lowest IPCE value. This value comprehends, therefore, inferior charge separation and transportation for the Ag_2S/BT photocatalyst causing destructive effect during the PEC performance. Comparison of our PCE efficiency with others in literatures, shows that our value for Ag_2O/BT exceeds Ti–$InCrO_6$ and Ti–$InCrO_6$ (1.7%) as well as 8% Ag_2O/$BiFeO_3$ (4.5%) [39–41]. The TiO_2-based $CsPbIBr_2$ device shows a lower efficiency of 5.02% [42] besides, the quantum dot-sensitized solar cells comprised of TiO_2 + CdS/CdSe/ZnS gives an efficiency equal 4.92% [43].

Fig. 9C shows the long-term stability data for DSSCs based on Ag_2O/BT and CuO/BT under continuous AM 1.5 G irradiation through a UV (<420 nm) cut-off filter at ca. 40°C. A little decrease in the efficiency was observed over the period of 800 h comprised of 3% and 9% for Ag_2O/BT and CuO/BT, respectively. This result clearly indicated that the DSSCs based on Ag_2O/BT was stable under visible-light irradiation at a relatively low temperature. The decrease was solely correlated to I_{SC} values and thus necessitated an increase in the optical absorption coefficients and as well as sunlight absorption of the DSSC. Fig. 9d shows an integrated Jsc of 4.0, 4.7, and 3.90 mA cm^{-2} for the devices made of bare BT, Ag_2O/BT and CuO/BT, respectively. These Jsc values are in harmony with the experimentally obtained Jsc for the constructed cells within the experimental uncertainties, which indicate the plausible method of fabrication.

3.7. Permittivity and AC conductivity

The variations of dielectric constant (ε') for the BT and those of the metal modified BT with frequencies from 100Hz to 10 MHz at 298K are illustrated in Fig. 10 (a). It shows that it decreased exponentially with increasing frequency. It can be noted that, at frequencies above 50 kHz, the dielectric constant is weak frequency dependent. The ε' versus frequency variation is explained based on Koop's and Maxwell-Wagner theories [44,45]. Dielectric constant decreases with increasing frequency, but a sudden decrease in ε' for all the samples in the low frequency region was observed due to different polarization mechanisms and small grain sizes. The polarization in nanomaterials is contributed by the alternate hopping of charge carriers between localized states and space charge polarization. The loading of Ag_2O, Ag_2S, and CuO on BT thickens the grain boundary, causing a decrease in the polarization and hence a decrease in ε'. The BT sample showed the highest dielectric constant (ε') compared to the other ones due to the interfacial charge transfer. At low frequency, the dielectric constant is caused by charge carriers' accumulation of and thus leads to surface charge polarization. The fast movement of electrons at low frequencies forces the electrons transfer all-over the electrode area and when it reaches the sample grain boundaries, a decrease in ε' is attained mostly at boosting the frequency. The decrease in dielectrics is explained by numerous types of polarization. At low frequencies, the increase in ε' is mainly caused by the simultaneous presence of ionic, electronic, space charge and interfacial polarization [46]. At high frequencies, the dipoles cannot rotate sufficiently rapidly and fail to follow the rapid changes in the applied electric field and thus leads to a decrease in dielectric constants due to the interfacial polarization [47]. The BT sample showed the highest dielectric constant (ε') compared to the other ones and accordingly they are arranged in the following order; [BT > Ag_2O-BT > Ag_2S-BT > CuO-BT]. Increasing the dielectric constant at low frequencies for the BT is indeed correlated to the charge lattice defect of space charge polarization [48].

Fig 10. b shows the dependence of the ac-conductivity (σ_{ac}) on the frequency (from 100 Hz to 10 MHz); at room temperature, for BT and CuO, Ag_2O and Ag_2S modified BT. It is clear from the Figure that σ_{ac} increases with increasing frequencies for the doped samples and they have the same trend, except that of the BT. The σ_{ac} of the BT decreases with frequencies up to 20 KHz due to the large polaron hopping [49], together with the short-range translational hopping of charge carriers between the localized states, and then increases with frequency. The ac conductivity increases with frequency, because as the frequency of the applied field increases, the conductive grains become more active due to increasing the hopping conduction. In addition, the hopping of small polaron type charge carriers among the localized states is another factor. This can be confirmed by studying the behavior of the frequency exponent;

$$\sigma_{AC} = A\,\omega^{s}$$

Where A is a constant, $\omega = 2\pi f$ is the angular frequency and s is the frequency exponent which determines the degree of interaction between mobile polaron and lattices [50]. The calculated values of *s* estimated from the slope of $\ln(\sigma_{ac})$ vs. $\ln(\omega)$ linear region were 0.971, 0.952, 0.875 and 0.113 for CuO-BT, Ag_2S-BT, Ag_2O-BT, and BT, respectively. This indicates the presence of major polaron conduction mechanism between metal ions with BT and rather affirms the existence of the hopping mechanism ($0 < s < 1$).

The BT shows the highest electrical conductivity that might correlate to the electronic exchange between tetravalent and trivalent titanium cations beside the C_3N_4 involvement; as depicted using XRD, FTIR and TEM-SAED results, followed in sequence by CuO-BT (18.6 nm), Ag_2O-BT (12.9 nm) and Ag_2S-BT (12.8 nm) nanomaterials. As the particle size decreased, the surface to volume ratio is increased with boosting the surface scattering that resulted in a reduction in the electrical conductivity [51]. Trapping of charge carriers due to increased defects might also be another reason of decreasing the conductivity [52]. Rising the conductivity at higher frequencies for modified BT samples confirmed the short range intra-well hopping of charge carriers between localized states. However, loading with silver oxides, an effective decrease in the number of charge carriers (Table 2) is terribly involved, hence

Table 2
Number of charge carrier density.

Sample	E_g (eV)	E_g (V)	exp	$n = AT^{3/2}e^{-Eg/2KT}$
BT	1.86	$1.86*10^{19}$	−22.61	$4.89*10^{18}$
CuO-BT	1.68	$1.68*10^{19}$	−20.42	$4.36*10^{19}$
Ag_2O-BT	1.74	$1.74*10^{19}$	−21.15	$2.10*10^{19}$
Ag_2S-BT	1.64	$1.64*10^{19}$	−19.93	$7.09*10^{19}$

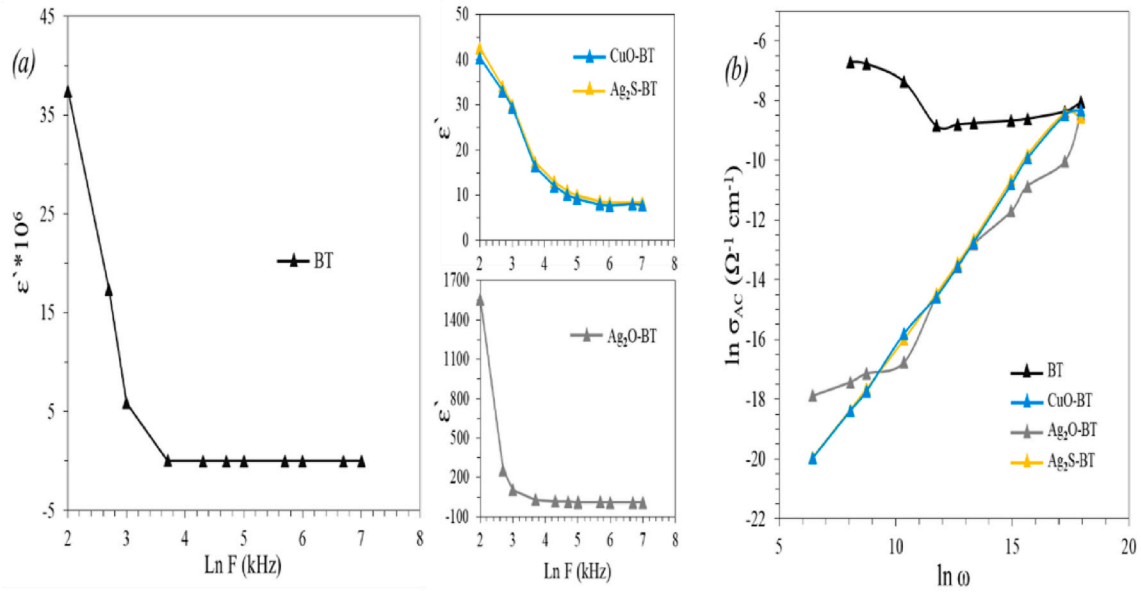

Fig. 10. *(a)* Dielectric permittivity as a function of frequency of the BT together with CuO-BT, Ag_2O-BT and Ag_2S-BT samples *(b)* AC Conductivity results of BT, CuO-BT, Ag_2O-BT and Ag_2S-BT samples at room temperature.

conductivity was found to decrease comparatively. The nonlinear behavior of the latter material is probably caused by inhomogeneous distributions of charge carriers. This behavior of the charge carriers is caused by the interaction between the imperfections created by the Ag_2O dopants and the TiO_{2-x} lattice. Doping reduces the conductivity based on the blocking barrier at the grain boundary as well as increasing its resistance [53,54]. The contradiction that the BT acquires high storage of charges as shown in dielectric constant (Fig. 10 a) however, presented lower number of charge carriers (Table 2) explains that the carriers mobility are relatively hindered. However, the dopants (Ag and Cu) those own low valence bands (deep acceptors) than TiO_2, beside oxygen vacancies and Ti^{3+} centres, prove higher mobility than BT and thus produce higher number of charge carriers. Although Ag_2S/BT presented the highest charge carrier numbers as it absorbs more light as depicted from UV, it offered no activity probably because of their severe recombination.

For investigating the active sites and redox behavior of the catalysts, The CV of the Ag_2O/BT electrode indicates two anodic peaks at 0.86 V and 0.74 V those correspondingly ascribed to Ag_2O and AgO moieties and they respectively give current densities of 2.6 and 2.0 mA cm^{-2} in the potential scan of -0.3–1.6 V (Fig. 11). In the reverse scan, two reduction peaks at 0.26 V (4.5 mA cm^{-2}) and 0.62 V (0.91 mA cm^{-2}) are depicted correlating the reduction cycle of AgO→Ag_2O→Ag, elucidating the formation of different active sites. Since the difference of ΔE (0.6 V) is deviated from 59 mV, then the reaction is considered as a quasi-reversible as also confirmed from deviating the value of Ipa/Ipc from 1 reflecting that the current is regulated mutually by the charge and mass transport. For comparison, the CV of the BT electrode depicts a reduction peak at a potential of 0.19 V due to Ti^{4+}/Ti^{3+} species giving a current density of 2.6 mA cm^{-2}. Shifting this peak into 0.26 V in Ag_2O/BT as well as increasing the current density boosts the involvement of more oxidized moieties Ag_2O/Ag_2O inside the BT. On the other hand, both CuO and Ag_2S incorporated BT indicate two redox peaks of reversibility nature inferring limited active sites as compared to Ag_2O/BT. This implicates that increasing the active sites of Ag_2O–AgO/BT compared to CuO and Ag_2S also takes part in enhancing the light collection and rather Ag manipulates the charges recombination probabilities. Boosting the efficiency result of the cell based Ag_2O is correlated to the evolution of Ag on Ag_2O beside AgO evidenced by CV and XPS results. This results in enhanced active sites, which function efficiently as visible-light photocatalyst assisted by lowering the band gap of Ag_2O. This is also supported by introducing Ti^{3+} of BT that heterostructured with g-C_3N_4. This promotes the separation of photogenerated carriers and rather accelerates the electron transfer as pointed by increasing the Voc values.

Correspondingly, the constructed Ag_2O/BT solar cell device was created by injecting the dye LUMO electrons subsequent to illumination into the Ag nanoparticles and then move into the conduction band of Ag_2O/BT interfaced with Ag metal. The energy-level diagram of the Ag_2O/BT is clarified in Scheme 2. Simultaneously, the oxidized dye receives an electron from the electrolyte (I^-) to restore the ground state of the dye. As shown, the evolved electrons will move to the FTO and then into the counter electrode. That electrode is going to give electrons to the cathode where it becomes transported to the electrolyte (I_3^-) so it is renovated.

4. Conclusion

The successful synthesis of TiO_{2-x} incorporated C_3N_4 was emphasized for the first-time using imidazole as a reducing agent. This

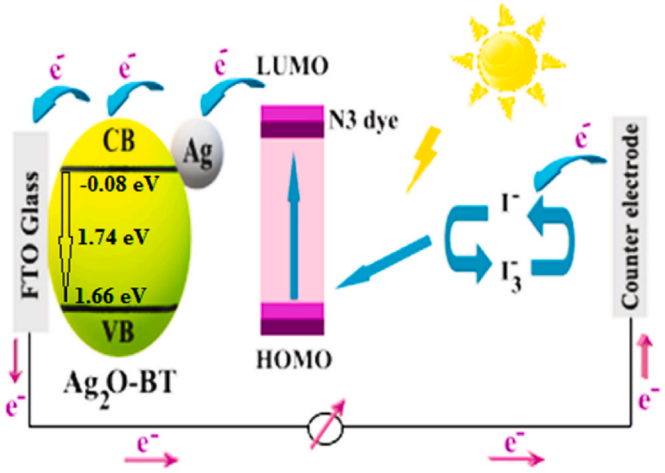

Scheme 2. Schematic diagram of the Ag_2O-BT nanocomposite photovoltaic response in DSSC.

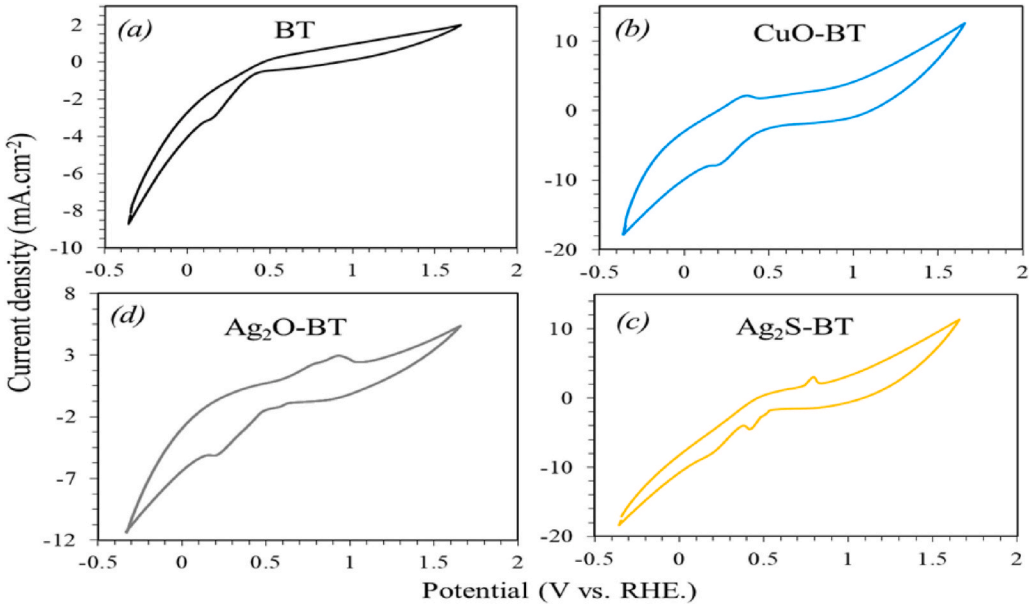

Fig. 11. Cyclic voltammetry (CV) curves of BT, CuO-BT, Ag_2O-BT and Ag_2S-BT catalysts at 50 mVs^{-1} in 1.0 M KCl.

heterostructure combination that has been emphasized using adverse techniques such as XPS, TEM-SAED, and FTIR showed marked PCE% when incorporated with P-type semiconductors especially Ag_2O (PCE = 6%) with improved stability. This catalyst has shown low band gap, high visible light absorption, high IPCE% in the correspondent margin, high increase in the surface area as well as growth number of active sites. Correlations of PCE% values with dielectrics and conductivities were well evaluated and discussed. Optimization of the C_3N_4 percentages to the black TiO_{2-x} is accomplished to highlight the role of the former in not only regulating the electron transfer and improving its transportation but also increasing the conductivity and monitoring the charges recombination.

CRediT authorship contribution statement

Nada A. Azab: Formal analysis, carried out the experimental part of the work, materials characterization helped in analyzing the data. **Z.A. Omran:** Formal analysis, helped in analyzing the conductivity data. **W. A.A. Bayoumy:** Formal analysis, Funding acquisition, helped in analyzing the conductivity data; data acquisition. Mohamed Mokhtar Mohamed, Formal analysis, analyzed the data; make correlations; writing manuscripts; deals with Journal submission.

Declaration of competing interest

The authors declare that they have no known competing financial interests or personal relationships that could have appeared to influence the work reported in this paper.

Appendix A. Supplementary data

Supplementary data to this article can be found online at https://doi.org/10.1016/j.solmat.2021.111347.

References

[1] W. Zhou, W. Li, J.Q. Wang, Y. Qu, Y. Yang, Y. Xie, K. Zhang, L. Wang, H. Fu, D. Zhao, Ordered mesoporous black TiO_2 as highly efficient hydrogen evolution photocatalyst, J. Am. Chem. Soc. 136 (2014) 9280–9283.

[2] N. Liu, C. Schneider, D. Freitag, M. Hartmann, U. Venkatesan, J. Müller, E. Spiecker, P. Schmuki, Black TiO_2 nanotubes: cocatalyst-free open-circuit hydrogen generation, Nano Lett. 14 (2014) 3309–3313.

[3] T. Su, Y. Yang, Y. Na, R. Fan, L. Li, L. Wei, B. Yang, W. Cao, An Insight into the role of oxygen vacancy in hydrogenated TiO_2 nanocrystals in the performance of dye-sensitized solar cells, ACS Appl. Mater. Interfaces 7 (2015) 3754–3763.

[4] H.-R. An, S.Y. Park, H. Kim, C.Y. Lee, S. Choi, S.C. Lee, S. Seo, E.C. Park, Y.-K. Oh, C.-G. Song, J. Won, Y.J. Kim, J. Lee, H.U. Lee, Y.-C. Lee, Advanced nanoporous TiO_2 photocatalysts by hydrogen plasma for efficient solar-light photocatalytic application, Sci. Rep. 6 (2016) 29683, https://doi.org/10.1038/srep29683.

[5] M. Allieta Naldoni, S. Santangelo, M. Marelli, F. Fabbri, S. Cappelli, C.L. Bianchi, R. Psaro, V.D. Santo, Effect of nature and location of defects on band gap narrowing in black TiO_2 nanoparticles, J. Am. Chem. Soc. 134 (2012) 7600–7603.

[6] X. Liu, G. Zhu, X. Wang, X. Yuan, T. Lin, F. Huang, Progress in black titania: a new material for advanced photocatalysis, Adv. Energy Mater. 6 (2016) 1600452–1600481.

[7] Y.H. Hu, A highly efficient photocatalyst—hydrogenated black TiO_2 for the photocatalytic splitting of water, Angew. Chem. Int. Ed. 51 (2012) 12410–12412.

[8] S. Chretien, H. Metiu, Electronic structure of partially reduced rutile TiO_2(110) surface: where are the unpaired electrons located? J. Phys. Chem. C 115 (2011) 4696–4705.

[9] H.-B. Fang, X.-H. Zhang, J. Wu, N. Li, Y.-Z. Zheng, X. Tao, Fragmented phosphorusdoped graphitic carbon nitride nanoflakes with broad sub-bandgap absorption for highly efficient visible-light photocatalytic hydrogen evolution, Appl. Catal. B Environ. 225 (2018) 397–405.

[10] K. Zhang, S. Ravishankar, M. Ma, G. Veerappan, J. Bisquert, F.F. Santiago, J. H. Park, Overcoming charge collection limitation at solid/liquid interface by a controllable crystal deficient overlayer, Adv. Energy Mater. 7 (2016) 1600923–1600930.

[11] X. Chen, S.S. Mao, Titanium dioxide nanomaterials: synthesis, properties, modifications, and applications, Chem. Rev. 7 (2007) 2891–2959.

[12] G. Rajender, P.K. Giri, Strain induced phase formation, microstructural evolution and bandgap narrowing in strained TiO_2 nanocrystals grown by ball milling, J. Alloys Compd. 676 (2016) 591–600.

[13] Q. Shi, G. Chai, W. Huang, Y. Shi, B. Huang, D. Wei, J. Qi, F. Su, W. Xuc, T. Lu, Fabrication of nanocrystalline λ-Ti_3O_5 with tunable terahertz wave transmission properties across a temperature induced phase transition, J. Mater. Chem. C 4 (2016) 10279–10285.

[14] R. Dadigala, R. Bandi, B.R. Gangapuramab, V. Guttena, Construction of in situ selfassembled $FeWO_4$/g-C_3N_4 nanosheet heterostructured Z-scheme photocatalysts for enhanced photocatalytic degradation of rhodamine B and tetracycline, Nanoscale Adv 1 (2019) 322–333.

[15] M.A.R. Dewan, G. Zhang, O. Ostrovski, Carbothermal reduction of a primary reduction of a primary ilmenite concentrate in different gas atmospheres, Metall. Mater. Trans. 41 (2010) 182–192.

[16] X. Liu, S. Gao, H. Xu, Z. Lou, W. Wang, B. Huang, Y. Dai, Green synthetic approach for Ti^{3+} self-doped TiO_{2-x} nanoparticles with efficient visible light photocatalytic activity, Nanoscale 5 (2013) 1870–1875.

[17] J. Yang, Progress of metal oxide (Sulfide)-Based photocatalytic materials for reducing nitrogen to ammonia, J. Chem. 2018 (2018) 3286782, https://doi.org/10.1155/2018/3286782.

[18] N.R. Dhineshbabu, V. Rajendran, N. Nithyavathy, R. Vetumperumal, Study of structural and optical properties of cupric oxide nanoparticles, Appl. Nanosci. 6 (2016) 933–939.

[19] C. Du, Y. Zhao, X. Liu, G. Shan, First-principles study of electronic properties of Cu doped Ag_2S, J. Phys.: Condens. Matter in press 30 (2018) 425502–425518.

[20] C. Fan, J. Miao, G. Xu, J. Liu, J. Lv, Y. Wu, Graphitic carbon nitride nanosheets obtained by liquid stripping as efficient photocatalysts under visible light, RSC Adv. 7 (2017) 37185–37193.

[21] Y. Xu, D. Chen, X. Jiao, Fabrication of CuO pricky microspheres with tunable size by a simple solution route, J. Phys. Chem. B 109 (2005) 13561–13566.

[22] M. Khairy, Mohamed Mokhtar Mohamed, S.M. Reda, A. Ibrahem, Effect of annealing temperature and Ag contents on the catalytic activity and supercapacitor performances of Ag@Ag_2O/RGO nanocomposites, Mater. Sci. Eng., B 242 (2019) 90–103.

[23] T. Kondratenko, O. Ovchinnikov, I. Grevtseva, M. Smirnov, O. Erina, V. Khokhlov, B. Darinsky, E. Tatianina, Thioglycolic acid FTIR spectra on Ag_2S quantum dots interfaces, Materials 13 (2020) 909, https://doi.org/10.3390/ma13040909.

[24] B. Bharti, S. Kumar, H.-N. Lee, R. Kumar, Formation of oxygen vacancies and Ti^{3+} state in TiO_2 thin film and enhanced optical properties by air plasma treatment, Sci. Rep. 6 (2016) 32355, https://doi.org/10.1038/srep32355.

[25] X. Liu, Z. Xing, H. Zhang, W. Wang, Y. Zhang, Z. Li, X. Wu, X. Yu, W. Zhou, Fabrication of 3D mesoporous black TiO_2/MoS_2/TiO_2 nanosheets for visible-light-driven photocatalysis, ChemSusChem 9 (2016) 1118–1124.

[26] M. Mohaia Bertótia, K. László, Surface modification of graphene and graphite by nitrogen plasma: determination of chemical state alterations and assignments by quantitative X-ray photoelectron spectroscopy, Carbon 84 (2015) 185–196.

[27] Z. Huanga, H. Chen, L. Zhao, W. Fang, X. He, W. Li, P. Tian, In suit inducing electron-donating and electron-withdrawing groups in carbon nitride by one-step NH_4Cl-assisted route: a strategy for high solar hydrogen production efficiency, Environ. Int. 126 (2019) 289–297.

[28] Z. Liu, C. Zhou, Improved photocatalytic activity of nano CuO-incorporated TiO_2 granules prepared by spray drying, PRO NAT SCI-MATER 25 (2015) 334–341.

[29] A.S. Ethiraj, D.J. Kang, Synthesis and characterization of CuO nanowires by a simple wet chemical method, Nanoscale Res. Lett. 7 (2012) 70. http://www.nanoscalereslett.com/content/7/1/70.

[30] L.Q. Wang, D.R. Baer, M.H. Engelhard, A.N. Shultz, The adsorption of liquid and vapor water on TiO_2 (110) surfaces: the role of defects, Surf. Sci. 344 (1995) 237–250.

[31] J.A.R. Herreraa, E. Mielczarskic, J. Mielczarskic, N.C. Castilloa, J. Kiwib, C. Pulgarina, Escherichia coli inactivation by N, S co-doped commercial TiO_2 powders under UV and visible light, Appl. Catal. B Environ. 84 (2008) 448–456.

[32] L. Shen, Z. Xing, J. Zou, Z. Li, X. Wu, Y. Zhang, Q. Zhu, S. Yang, W. Zhou, Black TiO_2 nanobelts/g-C_3N_4 nanosheets laminated heterojunctions with efficient visible-light-driven photocatalytic performance, Sci. Rep. 7 (2017) 41978, https://doi.org/10.1038/srep41978.

[33] J. Xu, Y. Chang, Y. Zhang, S. Ma, C. Xu, Effect of silver ions on the structure of ZnO and photocatalytic performance of Ag/ZnO composites, Appl. Surf. Sci. 255 (2008) 1996–1999.

[34] Al-Sarraj, K.M. Saoud, A. Elmel, S. Mansour, Y. Haik, Optoelectronic properties of highly porous silver oxide thin film SN Appl, Sciences 3 (2021) 15, https://doi.org/10.1007/s42452-020-04091-1.

[35] Y.W. Lu, X.W. Du, J. Sun, X. Han, Influence of surface Si–Ag bonds on photoluminescence of porous silicon, J. Appl. Phys. 100 (2006), 063512, https://doi.org/10.1063/1.2353397.

[36] A.M. Ibraheem, J. Kamalakkannan, Sustainable Scientific Advancements modified Ag_2O-ZnO thin films characterization and application of photocatalytic purification of carcinogenic dye in deionizer water and contaminated sea water solutions and Synthetic, Natural based Dye-Sensitized Solar Cells, Materials Science for Energy Technologies 3 (2020) 183–192.

[37] N. Aaron Deskins, Michel Dupuis, Intrinsic hole migration rates in TiO2 from density functional theory, J. Phys. Chem. C 113 (2009) 346–358. N. Wang, Y. Ma, J. Chen, C. Chen, H. San, J. Chenc, Z. Cheng, Defect-induced betavoltaic enhancement in black titania nanotube arrays, Nanoscale, 10 (2018) 13028-13036.

[38] S.G. Ullattil, A.V. Thelappurath, S.N. Tadka, J. Kavil, B.K. Vijayan, P. Periyat, A sol-solvothermal processed 'black TiO_2' as photoanode material in dye sensitized solar cells, Sol. Energy 155 (2017) 490–495.

[39] K. Kamalakkannan, V.L. Chandraboss, S. Prabha, B. Karthikeyan, S. Senthilvelan, Preparation and characterization of $TiInVO_6$-nanomaterial using precipitation method and its multiapplications, J. Mater. Sci. Mater. Electron. 27 (2015) 2488–2503.

[40] J. Kamalakkannan, V.L. Chandraboss, B. Loganathan, S. Prabha, B. Karthikeyan, S. Senthilvelan, $TiInCrO_6$-nanomaterial synthesis, characterization and multiapplications, Appl. Nanosci. 6 (2015) 691–702.
[41] T. Ahamad, A. Aldalbahi, S.M. Al shehri, S. Alotaibi, S. Alzahly, Z.-B. Wang, P. X. Feng, Enhanced photovoltaic performance of dye-sensitized solar cells based Ag2O doped BiFeO3 hetrostructures, Sol. Energy 220 (2021) 758–765.
[42] C.G. Koops, On the dispersion of resistivity and dielectric constant of some semiconductors at audiofrequencies, Phys. Rev. 83 (1951) 121–124.
[43] B. Yang, M. Wang, X. Hu, T. Zhou, Z. Zang, Highly efficient semitransparent CsPbIBr2 perovskite solar cells via low-temperature processed In2S3 as electron-transport-layer, Nanomater. Energy 57 (March 2019) 718–727.
[44] Q. Zhang, E. Uchaker, S.L. Candelariaz, G. Cao, Nanomaterials for energy conversion and storage, Chem. Soc. Rev. 42 (2013) 3127–3172.
[45] K.W. Wagner, The distribution of relaxation times in typical dielectrics, Ann. Phys. 40 (1973) 817–819.
[46] G.G. Raju, Dielectrics in Electric Fields, Marcel Dekker Inc., New York, 2003, https://doi.org/10.1201/9780203912270.
[47] S.G. Kakade, Y.R. Ma, R.S. Devan, Y.D. Kolekar, C.V. Ramana, Dielectric, complex impedance, and electrical transport properties of erbium (Er^{3+}) ion-substituted nanocrystalline, cobalt-rich ferrite ($Co_{1.1}Fe_{1.9-x}Er_xO_4$), *J. Phys. Chem.* C 120 (2016) 5682–5693.
[48] S. Saafan, S. Assar, S. Mansour, Magnetic and electrical properties of Co_{1-X} Ca_X Fe_2O_4 nanoparticles synthesized by the auto combustion method, J. Alloy Compd. 542 (2012) 192–198.
[49] I.G. Austin, N.F. Mott, Polarons in crystalline and non-crystalline materials, Adv. Phys. 18 (1969) 41–102.
[50] A.K. Jonscher, A new understanding of the dielectric relaxation of solids, J. Mater. Sci. 16 (1981) 2037–2060.
[51] K. Karthik, S. Kesavapandian, N.V. Jaya, Effect of nickel doping on structural, optical and electrical properties of TiO_2 nanoparticles by sol–gel method, Appl. Surf. Sci. 256 (2010) 6829–6833.
[52] S. Manjunatha, A.K. Koppalkarb, M.V.N. Ambika Prasad, Dielectric spectroscopy of polyaniline/stanic oxide (PANI/SnO_2) composites, Ferroelectrics 366 (2010) 22–28.
[53] Q.A. Acton, Issues in Hydrogen, Fuel Cell, Eectrochemical, and Experimental Technologies, Scholarly Editions, 2013, pp. 343–350.
[54] R.J.D. Tilley, Defects in Solids, Wiley-Interscience, 2008, pp. 352–354, https://doi.org/10.1002/9780470380758.